Scale dependent crystal plasticity framework with dislocation density and grain boundary effects

L.P. Evers [a,b], W.A.M. Brekelmans [b,*], M.G.D. Geers [b]

[a] *Netherlands Institute for Metals Research (NIMR), P.O. Box 5008, 2600 GA Delft, The Netherlands*
[b] *Eindhoven University of Technology, Section of Materials Technology, Department of Mechanical Engineering, P.O. Box 513, 5600 MB Eindhoven, The Netherlands*

Abstract

The geometrically non-linear scale dependent response of polycrystal FCC metals is modelled by an enhanced crystal plasticity framework based on the evolution of several dislocation density types and their distinct physical influence on the mechanical behaviour. The isotropic hardening contribution follows from the evolution of statistically stored dislocation (SSD) densities during plastic deformation, where the determination of the slip resistance is based on the mutual *short range* interactions between all dislocation types, i.e. including the geometrically necessary dislocation (GND) densities. Moreover, the GND's introduce *long range* interactions by means of a back-stress measure, opposite to the slip system resolved shear stress.

The grain size dependent mechanical behaviour of a limited collection of grains under plane stress loading conditions is determined using the finite element method. Each grain is subdivided into finite elements and an additional expression, coupling the GND densities to spatial crystallographic slip gradients, renders the GND densities to be taken as supplemental nodal degrees of freedom. Consequently, these densities can be uncoupled at the grain boundary nodes, allowing for the introduction of grain boundary dislocations (GBD's) based on the lattice mismatch between neighbouring grains and enabling the obstruction of crystallographic slip perpendicular to the grain boundary.
© 2004 Elsevier Ltd. All rights reserved.

Keywords: Strain gradient; Crystal plasticity; Scale effects; Dislocations; Grain boundaries

1. Introduction

The grain size dependent mechanical behaviour of a polycrystal FCC metal has been modelled physically using a crystal plasticity approach for finite deformations. In most conventional single and polycrystal plasticity models, e.g. as published by Bronkhorst et al. (1992) and Kalidindi et al. (1992), the influence of

---

inter- and intragranular inhomogeneities is not explicitly incorporated in the constitutive description, whereas it is the basic origin of scale dependent behaviour and the resulting size effects. In general, such inhomogeneities at the microscale can be caused by externally applied macroscopic gradients of plastic deformation, by the presence of grain boundaries locally obstructing the plastic deformation (Becker and Panchanadeeswaran, 1995), or by a combination of both. The best-known macroscopic experimental consequence of these effects is the increased flow stress on decreasing average grain size, which is expressed by the so-called "Hall–Petch relation" (Hall, 1951; Petch, 1953; Armstrong et al., 1962). In particular, the flow stress is nearly proportional to the inverse square root of the average grain diameter (see also Hansen, 1982; Narutani and Takamura, 1991; Evers et al., in press).

Several suggestions have been proposed to explain this strengthening effect (Gavriljuk et al., 1999). The "dislocation pile-up models" are based on the perception that dislocations pile-up against grain boundaries and therefore obstruct the crystallographic slip through stress concentrations. On the other hand, "work hardening models" state that the overall concentration of dislocations in a grain increases once the volume in which they reside —which is connected to the grain size— decreases, corresponding to an increased inhomogeneity and a decreased mean free path within the grains. The presented model actually includes both effects, because dislocations concentrate at the grain boundaries and inflict a back-stress to the motion of dislocations carrying the plastic deformation, while at the same time, the strength of those dislocation concentrations depends on the heterogeneity within the grain, which increases with decreasing grain size.

Next to the so-called "geometrically necessary dislocations" (GND's), which are directly related to local non-uniform plastic deformations and which are required to preserve the compatibility of the crystallographic lattice in cases of unevenly distributed plastic slip, the second type of dislocations to be distinguished are "statistically stored dislocations" (SSD's), a distinction first identified by Ashby (1970). The latter dislocation density accumulates during (uniform as well as non-uniform) plastic deformation as a result of interactions between dislocations mutually, and the motion of SSD's is actually the mechanism behind crystallographic (plastic) slip on the distinct slip planes of the material. It can be expected that the GND's are concentrated near the grain boundary regions (Kocks, 1970; Thompson et al., 1973), due to the lattice mismatch with neighbouring grains, whereas the SSD densities mostly evolve in the grain interiors, as a result of the more intensive and less obstructed plastic flow in that region. An investigation of the interaction between dislocation densities and grain boundaries can be found in Ashmawi and Zikry (2003).

The actual difference between SSD's and GND's resides in their role only, i.e. in the fact that the latter do not directly participate in the local crystallographic slip, yet they emerge as a (non-local) result of spatial gradients of that slip. A second (resulting) difference between both types of dislocations is the sign and the variation of that sign in space. The SSD's, due to their statistical nature, have a more or less random sign observed at a length scale associated with the grain structures, as a result of which any bias cancels out and the SSD's do not contribute to any in-homogeneities. The sign of the GND densities has a profound geometrical impact and therefore a larger periodicity, as it is coupled to specific lattice curvatures and distortions. The actual identification of a certain dislocation as being a statistically stored one or a geometrically necessary one, however, remains rather ambiguous (since at the level of a single dislocation there is no physical difference), as well as keeping track of the process of dislocations switching between both types. Nevertheless, when the *densities* of both types are considered, a clear distinction can be made based on their characteristics, i.e. the GND density equals the minimum density (or local surplus of a certain sign) in order to accommodate the local plastic strain gradients, whereas the remaining density is considered to be statistically stored (Gao and Huang, 2003).

After establishing the occurrence of both dislocation types, the entire framework is furnished to account for their distinct effect on the constitutive behaviour, incorporating any number or type (edge or screw) of dislocations. In general local continuum crystal plasticity models, the presence, motions, and interactions of

dislocations are not explicitly distinguished, as only their effects are modelled indirectly by a phenomenological slip law and hardening evolution. The present framework (partly adopted from Evers et al., 2002) still incorporates a phenomenological slip law, however it is enhanced and the slip resistance is entirely based on short-range interactions between all (SSD as well as GND) dislocations intersecting the current slip system (Franciosi and Zaoui, 1982). Now, the accumulation of dislocations —related to the history of crystallographic slip— is the driving force behind the isotropic hardening term. Furthermore, a second extension is introduced to account for the distinct influence of the GND densities on the plastic slip in a long-range sense, i.e. through a back-stress measure, counteracting the local resolved shear stress and related to the heterogeneity of the GND field after removal of external loads. This provides for a physically motivated and consistent incorporation of global as well as local (intragranular) strain gradient effects and hence also of scale dependent effects such as grain size dependent responses.

Next to grain size effects and related size effects under micro-torsion (Fleck et al., 1994), the prediction of particle size effects (Ashby, 1970) and indenter size effects (Nix and Gao, 1998; Gao et al., 1999) is still the objective of ongoing study (e.g. Aifantis, 1987; Fleck and Hutchinson, 1997; Shu and Fleck, 1999), using so-called "strain gradient models". Such approaches introduce an intrinsic material length scale in an analytical plasticity formulation, relying on the underlying generation and distribution of dislocations. Furthermore, continuum theories of dislocations have been formulated to further enhance those strain gradient models (Dai and Parks, 1997; Steinmann, 1996; Sluys and Estrin, 2000; Acharya, 2001; Bassani, 2001; Gurtin, 2002; Cermelli and Gurtin, 2002) by making use of (global) plastic or elastic incompatibilities, based on the work of Nye (1953). In the present work, as a further enhancement, the densities and their influence are solely and explicitly determined on the FCC slip systems, at a scale that includes global as well as local strain gradients. A comparison of simulations using the actual model to the discrete dislocation predictions of a constrained strip under simple shear for the case of double slip (Shu et al., 2001) can be found in Evers et al. (in press). Furthermore, Gurtin (2002) and Cermelli and Gurtin (2002) have developed a framework that is based on similar hypotheses as the one presented here, yet based on energetic considerations.

It is emphasized that in the present concept, the grain size does not explicitly enter the constitutive model and the model parameters can be kept constant throughout the entire grain. The grain size effect arises naturally as a result of intragranular heterogeneities affected by incompatibilities and obstructions at the grain boundaries. When the grain size is taken smaller, the inhomogeneities increase. Nevertheless, the primary length parameter entering the presented model is the length of the Burgers vector, which relates the plastic strain gradients to the GND densities at slip system level. Moreover, limiting the GND effect to an increased hardening rate or slip resistance near the grain boundaries (Worthington and Smith, 1964; Gray III et al., 1999) is not satisfactory, as clearly remarked by Mughrabi (2001), stating that a simple superposition of the GND density on the SSD density does not suffice. Microbending tests (Fleck et al., 1994; Stölken and Evans, 1998) suggest that the GND density can be substantially smaller than the SSD density, even though their contribution may be quite significant or even dominant.

In the next section, the entire crystal plasticity framework is presented, which covers the general constitutive formulation including an extended slip law, the determination of the entries in that slip law, i.e. the slip resistance and the back-stress, and finally the evolution equations for the SSD, GND, and "grain boundary dislocation" (GBD) densities. Next, in Section 3, the large deformation implementation of the entire model is discussed under the assumption of plane stress. Regarding the finite element formulation, the complete algorithmic framework is addressed, i.e. ranging from the integration point solutions up till the incremental-iterative solution of the global set of non-linear equations. Finally, in Section 4, the response of a polycrystal FCC metal (consisting of 12 grains) under plane stress deformation is simulated, of which the grain size effect on the response and the intragranular variations of several quantities is demonstrated.

2. Crystal plasticity model

2.1. Constitutive framework

Point of departure is the classical multiplicative decomposition of the deformation gradient tensor into an elastic and a plastic part according to (Lee, 1969)

$$\boldsymbol{F} = \boldsymbol{F}_{\mathrm{e}} \cdot \boldsymbol{F}_{\mathrm{p}}, \tag{1}$$

where the elastic deformation includes small lattice deformations and possibly large rigid body rotations. Next, the second Piola–Kirchhoff stress measure $\boldsymbol{\tau} \equiv \det(\boldsymbol{F}_{\mathrm{e}}) \boldsymbol{F}_{\mathrm{e}}^{-1} \cdot \boldsymbol{\sigma} \cdot \boldsymbol{F}_{\mathrm{e}}^{-\mathrm{T}}$, with respect to the stress-free intermediate configuration (Mandel, 1974), is taken to be elastically related to its work conjugated elastic Green strain measure $\boldsymbol{E}_{\mathrm{e}}$ through

$$\boldsymbol{\tau} = {}^{4}\boldsymbol{C} : \boldsymbol{E}_{\mathrm{e}}, \quad \boldsymbol{E}_{\mathrm{e}} \equiv \frac{1}{2}(\boldsymbol{C}_{\mathrm{e}} - \boldsymbol{I}), \quad \boldsymbol{C}_{\mathrm{e}} \equiv \boldsymbol{F}_{\mathrm{e}}^{\mathrm{T}} \cdot \boldsymbol{F}_{\mathrm{e}}, \tag{2}$$

where $\boldsymbol{\sigma}$ is the Cauchy stress tensor, $\boldsymbol{C}_{\mathrm{e}}$ is the elastic right Cauchy–Green deformation tensor and $\boldsymbol{I}$ is the second-order unit tensor. The fourth-order isotropic elasticity tensor ${}^{4}\boldsymbol{C}$ is defined by Young's modulus $\boldsymbol{E}$ and Poisson's ratio v.

Furthermore, the evolution of the plastic deformation is prescribed by the plastic velocity gradient tensor $\boldsymbol{L}_{\mathrm{p}}$, which by definition can be written as the sum of all crystallographic slip rates $\dot{\gamma}^{\alpha}$ on the 12 $\{1\,1\,1\}\langle 1\,1\,0\rangle$ slip systems α of the FCC metal according to (Rice, 1971)

$$\dot{\boldsymbol{F}}_{\mathrm{p}} = \boldsymbol{L}_{\mathrm{p}} \cdot \boldsymbol{F}_{\mathrm{p}}, \quad \boldsymbol{L}_{\mathrm{p}} = \sum_{\alpha} \dot{\gamma}^{\alpha} \boldsymbol{P}_{0}^{\alpha}, \quad \boldsymbol{P}_{0}^{\alpha} \equiv \boldsymbol{m}_{0}^{\alpha} \boldsymbol{n}_{0}^{\alpha}, \quad \alpha = 1, 2, \ldots, 12. \tag{3}$$

Here, $\boldsymbol{P}_{0}^{\alpha}$ is the non-symmetric Schmid tensor, represented in the reference configuration as the dyadic product of the two orthonormal vectors $\boldsymbol{m}_{0}^{\alpha}$ and $\boldsymbol{n}_{0}^{\alpha}$, the slip direction and slip plane normal, respectively.

The above elastic and plastic parts are coupled through a viscoplastic flow rule (Hutchinson, 1976; Peirce et al., 1982), which is defined for each slip system α and specifies the rate of plastic shearing $\dot{\gamma}^{\alpha}$ as a function of the associated "effective" shear stress $\tau_{\mathrm{eff}}^{\alpha}$ and the current slip resistance s^{α} (see also Nemat-Nasser et al., 1998; Harder, 1999; Kocks, 2001; Evers et al., in press)

$$\dot{\gamma}^{\alpha} = \dot{\gamma}_{0} \left(\frac{|\tau_{\mathrm{eff}}^{\alpha}|}{s^{\alpha}} \right)^{\frac{1}{m}} \exp\left\{ -\frac{G_{0}}{kT} \left(1 - \frac{|\tau_{\mathrm{eff}}^{\alpha}|}{s^{\alpha}} \right) \right\} \mathrm{sign}(\tau_{\mathrm{eff}}^{\alpha}), \tag{4}$$

where $\dot{\gamma}_{0}$ and m are material parameters representing the reference plastic strain rate and the rate sensitivity exponent, k is Boltzmann's constant, T is the absolute temperature, and G_{0} is the total free energy needed for a moving dislocation to overcome a short-range barrier without the aid of external work. Furthermore, the effective stress $\tau_{\mathrm{eff}}^{\alpha}$ is defined as the difference between the resolved shear stress τ^{α} (also known as "Schmid stress") and the resolved back-stress $\tau_{\mathrm{b}}^{\alpha}$

$$\tau_{\mathrm{eff}}^{\alpha} = \tau^{\alpha} - \tau_{\mathrm{b}}^{\alpha}, \quad \tau^{\alpha} \equiv \boldsymbol{\tau} : \boldsymbol{P}_{0}^{\alpha}, \quad \tau_{\mathrm{b}}^{\alpha} \equiv \boldsymbol{\tau}_{\mathrm{b}} : \boldsymbol{P}_{0}^{\alpha}, \tag{5}$$

where both resolved stress measures are projections (Asaro and Rice, 1977; Bronkhorst et al., 1992) of their corresponding stress tensors $\boldsymbol{\tau}$ and $\boldsymbol{\tau}_{\mathrm{b}}$ (Harder, 1999) on slip system α, respectively.

2.2. Dislocation interactions

The concepts above leave the slip system strengths and the back-stress tensor still to be determined. The back-stress tensor describes the effect of long-range stresses caused by the heterogeneity of the GND field, whereas the slip resistances are a measure for the impeding of dislocation movement by the formation of

short-range interactions between both SSD's and GND's residing on coplanar or intersecting slip systems. The type and number of short-range interactions can be quantified through a set of interaction coefficients, stored in the interaction matrix $A^{\alpha\xi}$ (Franciosi and Zaoui, 1982), after which the slip system strength s^α is taken proportional to the square root of the effective obstacle density following Ashby (1970)

$$s^\alpha = c\mu b \sqrt{\sum_\xi A^{\alpha\xi}|\rho_{\mathrm{SSD}}^\xi| + \sum_\xi A^{\alpha\xi}|\rho_{\mathrm{GND}}^\xi|}. \tag{6}$$

In here, c is a constant ranging from 0.05 to 2.6 for different materials (Lavrentev, 1980), μ is the shear modulus and b is the length of the Burgers vector. Furthermore, when considering FCC metals, ρ_{SSD}^ξ and ρ_{GND}^ξ stand for the 12 edge SSD densities ($\xi = 1, 2, \ldots, 12$) and the 12 edge and 6 screw GND densities ($\xi = 1, 2, \ldots, 18$), respectively (Kubin et al., 1992). A complete listing of the different dislocation densities, including their type, orientation, and corresponding slip system, is specified in Table 1.

The global back-stress tensor is defined in the reference configuration and is composed of the resulting long-range shear stress contributions (τ_{e}^α and τ_{s}^α of the particular edge and screw GND density field, respectively) on the respective slip systems α according to (Harder, 1999)

$$\boldsymbol{\tau}_{\mathrm{b}} = \sum_\alpha -(\tau_{\mathrm{e}}^\alpha + \tau_{\mathrm{s}}^\alpha)(\boldsymbol{P}_0^\alpha + \boldsymbol{P}_0^{\alpha\mathrm{T}}), \tag{7}$$

where the account for their spatial orientation through $\boldsymbol{P}_0^\alpha$ (cf. Eq. (3)) leads to a secondary resolved back-stress contribution on the other slip systems after employing Eq. (5). Note that the minus sign in this

Table 1
List of indices and vectors for dislocation densities and slip systems used in the simulation of FCC metals; the Schmid and Boas notation is discussed in Franciosi and Zaoui (1982). b is the length of the Burgers vector $\boldsymbol{b}$

Dislocation density ξ	Type	Slip system α	$\boldsymbol{m}$ or $\frac{\boldsymbol{b}}{b}$	$\boldsymbol{n}$	Schmid and Boas
1	Edge	1	$\frac{1}{\sqrt{2}}[\bar{1}\,1\,0]$	$\frac{1}{\sqrt{3}}[1\,1\,1]$	B5
2	Edge	2	$\frac{1}{\sqrt{2}}[1\,0\,\bar{1}]$	$\frac{1}{\sqrt{3}}[1\,1\,1]$	−B4
3	Edge	3	$\frac{1}{\sqrt{2}}[0\,\bar{1}\,1]$	$\frac{1}{\sqrt{3}}[1\,1\,1]$	B2
4	Edge	4	$\frac{1}{\sqrt{2}}[\bar{1}\,\bar{1}\,0]$	$\frac{1}{\sqrt{3}}[1\,1\,\bar{1}]$	A6
5	Edge	5	$\frac{1}{\sqrt{2}}[1\,0\,1]$	$\frac{1}{\sqrt{3}}[1\,1\,\bar{1}]$	−A3
6	Edge	6	$\frac{1}{\sqrt{2}}[0\,1\,\bar{1}]$	$\frac{1}{\sqrt{3}}[1\,1\,\bar{1}]$	A2
7	Edge	7	$\frac{1}{\sqrt{2}}[1\,1\,0]$	$\frac{1}{\sqrt{3}}[\bar{1}\,1\,\bar{1}]$	−D6
8	Edge	8	$\frac{1}{\sqrt{2}}[\bar{1}\,0\,1]$	$\frac{1}{\sqrt{3}}[\bar{1}\,1\,\bar{1}]$	−D4
9	Edge	9	$\frac{1}{\sqrt{2}}[0\,\bar{1}\,\bar{1}]$	$\frac{1}{\sqrt{3}}[\bar{1}\,1\,\bar{1}]$	D1
10	Edge	10	$\frac{1}{\sqrt{2}}[1\,\bar{1}\,0]$	$\frac{1}{\sqrt{3}}[\bar{1}\,\bar{1}\,1]$	−C5
11	Edge	11	$\frac{1}{\sqrt{2}}[\bar{1}\,0\,\bar{1}]$	$\frac{1}{\sqrt{3}}[\bar{1}\,\bar{1}\,1]$	−C3
12	Edge	12	$\frac{1}{\sqrt{2}}[0\,1\,1]$	$\frac{1}{\sqrt{3}}[\bar{1}\,\bar{1}\,1]$	C1
13	Screw	–	$\frac{1}{\sqrt{2}}[1\,\bar{1}\,0]$	$\frac{1}{\sqrt{3}}[1\,\bar{1}\,\bar{1}]$ or $\frac{1}{\sqrt{3}}[\bar{1}\,1\,\bar{1}]$	−A6 or −D6
14	Screw	–	$\frac{1}{\sqrt{2}}[1\,0\,1]$	$\frac{1}{\sqrt{3}}[1\,\bar{1}\,\bar{1}]$ or $\frac{1}{\sqrt{3}}[\bar{1}\,\bar{1}\,1]$	−A3 or C3
15	Screw	–	$\frac{1}{\sqrt{2}}[0\,1\,1]$	$\frac{1}{\sqrt{3}}[\bar{1}\,1\,\bar{1}]$ or $\frac{1}{\sqrt{3}}[\bar{1}\,\bar{1}\,1]$	−D1 or C1
16	Screw	–	$\frac{1}{\sqrt{2}}[\bar{1}\,1\,0]$	$\frac{1}{\sqrt{3}}[1\,1\,1]$ or $\frac{1}{\sqrt{3}}[\bar{1}\,1\,\bar{1}]$	B5 or D4
17	Screw	–	$\frac{1}{\sqrt{2}}[1\,0\,\bar{1}]$	$\frac{1}{\sqrt{3}}[1\,1\,1]$ or $\frac{1}{\sqrt{3}}[\bar{1}\,1\,\bar{1}]$	−B4 or D4
18	Screw	–	$\frac{1}{\sqrt{2}}[0\,\bar{1}\,1]$	$\frac{1}{\sqrt{3}}[1\,1\,1]$ or $\frac{1}{\sqrt{3}}[1\,\bar{1}\,\bar{1}]$	B2 or −A2

equation accounts for the transformation of the resulting long-range shear stress contributions to back-stress contributions in Eq. (5).

The determination of the resolved long-range shear stress contributions τ_e^α and τ_s^α in the undeformed configuration originally stems from the equations for the stress concentration near individual edge and screw dislocations by Cottrell (1961). However, when applying those equations to determine the resulting long-range stress state in a certain origin as caused by a uniform field of GND's, it completely cancels out. This is caused by the fact that each individual dislocation has a counterpart with an exact opposite contribution to the resulting long-range stress. Therefore, not the GND density field itself, but its spatial variations cause resulting long-range stresses.

In order to quantify that effect, the resulting long-range stress at slip system α for the edge and screw GND densities is computed by an analytical integration procedure of the equations for individual dislocations (Cottrell, 1961) over a circular domain with radius R around the origin, while the GND densities are assumed to vary linearly in space.

$$\tau_e^\alpha = -\frac{\mu b R^2}{8(1-v)} \sum_\xi d_e^{\alpha\xi} (\nabla_0 \rho_{GND}^\xi \cdot \boldsymbol{m}_0^\alpha), \tag{8}$$

$$\tau_s^\alpha = \frac{\mu b R^2}{4} \sum_\xi d_s^{\alpha\xi} (\nabla_0 \rho_{GND}^\xi \cdot p_0^\alpha), \quad \boldsymbol{p}_0^\alpha = \boldsymbol{m}_0^\alpha \times \boldsymbol{n}_0^\alpha. \tag{9}$$

Here, the multipliers $d_e^{\alpha\xi}$ and $d_s^{\alpha\xi}$ equal -1, 0, or 1, according to the way the dislocation type ξ spatially relates to the slip system α (cf. Table 1)

$$d_e^{\alpha\xi} = \begin{cases} 1 & \text{for } \alpha = \xi = 1, 2, \ldots, 12 \\ 0 & \text{for all other cases} \end{cases} \tag{10}$$

$$d_s^{\alpha\xi} = \begin{cases} -1 & \text{for } d_s^{(4,13)}, d_s^{(6,18)}, d_s^{(8,17)}, d_s^{(9,15)} d_s^{(10,16)}, d_s^{(11,14)} \\ 1 & \text{for } d_s^{(1,16)}, d_s^{(2,17)}, d_s^{(3,18)}, d_s^{(5,14)} d_s^{(7,13)}, d_s^{(12,15)} \\ 0 & \text{for all other cases.} \end{cases} \tag{11}$$

2.3. Dislocation densities

In the remainder of this section, the determination of the SSD, GND and GBD densities is discussed. First, the evolution of the 12 edge SSD densities of the FCC metal, as required in Eq. (6), is based on the balance between the accumulation and annihilation rates, expressed by

$$\dot{\rho}_{SSD}^\xi = \frac{1}{b} \left(\frac{1}{d_e^{\alpha\xi} L^\alpha} - 2 y_c \rho_{SSD}^\xi \right) d_e^{\alpha\xi} |\dot{\gamma}^\alpha|, \quad \rho_{SSD}^\xi(t=0) = \rho_{SSD_0}, \tag{12}$$

which is a generalisation of the relation originally proposed by Essmann and Mughrabi (1979). The accumulation rate (first term in the right-hand side of Eq. (12)) is linked to the average dislocation segment length of mobile dislocations (SSD's) on system α, L^α, which is strongly related to the current dislocation state through (Tabourot et al., 1997; Arsenlis and Parks, 2002)

$$L^\alpha = \frac{K}{\sqrt{\sum_\xi H^{\alpha\xi} |\rho_{SSD}^\xi| + \sum_\xi H^{\alpha\xi} |\rho_{GND}^\xi|}}. \tag{13}$$

Here, K is a constant and the coefficients $H^{\alpha\xi}$ indicate the mutual immobilisation between dislocations of different slip systems, following the same convention as $A^{\alpha\xi}$ in Eq. (6), yet having different values. Fur-

thermore, the annihilation rate (second contribution in the right-hand side of Eq. (12)) is assumed to be controlled by the critical annihilation length y_c, a material parameter characterising the average distance between two dislocations of opposite sign which triggers spontaneous neutralization.

Next, the GND density is determined from the gradients of the crystallographic slip in the undeformed situation from geometrical compatibility (Nye, 1953; Kröner, 1962; Ashby, 1970; Arsenlis and Parks, 2002)

$$\rho_{\text{GND}}^{\xi} = \rho_{\text{GND}_0}^{\xi} - \frac{1}{b} \sum_{\alpha} d_e^{\alpha\xi} (\nabla_0 \gamma^{\alpha} \cdot \boldsymbol{m}_0^{\alpha}) + \frac{1}{b} \sum_{\alpha} d_s^{\alpha\xi} (\nabla_0 \gamma^{\alpha} \cdot \boldsymbol{p}_0^{\alpha}). \tag{14}$$

For FCC metals, in contrast to the 12 positive SSD densities, the 12 edge and 6 screw GND densities have a certain polarity which is crucial to ascertain the direction of the slip system resolved back-stress. As can be clearly seen from Eq. (14), the sign of the GND densities is directly related to the sign of the corresponding crystallographic slip gradients. Each of the 6 screw dislocation densities is determined by addition of the appropriate slip gradients on *both* the glide planes in which they can reside, as they are assumed to be free to cross-slip while their corresponding slip plane remains an ambiguous choice. This is consistent with the fact that in Eq. (11), each (screw) dislocation density (ξ) has two contributing slip systems (α), whose orientations can be found in Table 1. Furthermore, the initial GND density $\rho_{\text{GND}_0}^{\xi}$ can be identified with the initial grain boundary dislocation density field, present before the onset of plastic deformation. The GBD densities are introduced to account for lattice incompatibilities across grain boundaries. Because of their geometrical nature, the GBD densities have similar constitutive influences as the GND densities. Therefore, as a part of $\rho_{\text{GND}_0}^{\xi}$, the 12 edge GND densities are taken equal to the initial grain boundary dislocation (GBD) densities

$$\rho_{\text{GND}_0}^{\xi} \equiv d_e^{\alpha\xi} \rho_{\text{GBD}}^{\alpha}. \tag{15}$$

This contribution is emphasized to be of qualitative nature, as the exact determination of the GBD densities, including the screw dislocations, is evidently more complicated than captured by the trends using the present simplified formulation, visualised in Fig. 1.

To determine the GBD density, first, the slip system orientations of two adjacent grains α and β are evaluated. In order to account for the symmetries of the FCC lattice, the slip systems of grain α are related to the particular slip system configuration of grain β, as indicated in Table 2, that provides the best overall correspondence between all slip systems on either side, i.e. resulting in the smallest amount of GBD densities. Next, the GBD density is related to the misfit length h^{α} between the slip system under consideration of grain α and its associate slip system of grain β, where h^{α} follows by comparing the lengths of their grain boundary resolved Burgers vectors, b^{α} and b^{β}, respectively, according to

$$|\rho_{\text{GBD}}^{\alpha}| \equiv \frac{1}{h^{\alpha 2}} = \left(\frac{1}{b^{\alpha}} - \frac{1}{b^{\beta}} \right)^2. \tag{16}$$
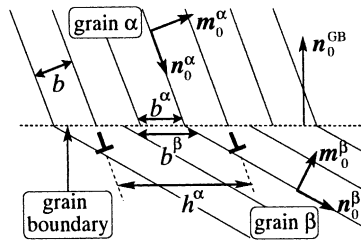

Fig. 1. A grain boundary lattice mismatch gives rise to additional (GBD) dislocations; the GBD density is determined from the lengths of the grain boundary resolved Burgers vector (b^{α} and b^{β}) and the direction of the grain boundary unit normal $\boldsymbol{n}_0^{\text{GB}}$.

Table 2
The slip systems of grain α in the first row correspond to one of the slip system configurations of grain β in the consecutive rows, in accordance with the best geometrical match, depending on mutual orientation differences

Grain α	1	2	3	4	5	6	7	8	9	10	11	12
Related slip	1	2	3	4	5	6	7	8	9	10	11	12
systems	2	3	1	11	12	10	5	6	4	8	9	7
of grain β	3	1	2	9	7	8	12	10	11	6	4	5
	4	5	6	1	2	3	10	11	12	7	8	9
	5	6	4	8	9	7	2	3	1	11	12	10
	6	4	5	12	10	11	9	7	8	3	1	2
	7	8	9	10	11	12	1	2	3	4	5	6
	8	9	7	5	6	4	11	12	10	2	3	1
	9	7	8	3	1	2	6	4	5	12	10	11
	10	11	12	7	8	9	4	5	6	1	2	3
	11	12	10	2	3	1	8	9	7	5	6	4
	12	10	11	6	4	5	3	1	2	9	7	8

When considering the grain boundary unit normal $\boldsymbol{n}_0^{\mathrm{GB}}$ to be pointed from the grain having the largest grain boundary resolved Burgers vector to the grain having the smallest one, the sign and magnitude of the GBD density can be expressed by

$$\rho_{\mathrm{GBD}}^{\alpha} = \mathrm{sign}(\boldsymbol{n}_0^{\alpha} \cdot \boldsymbol{n}_0^{\mathrm{GB}}) \frac{(|\boldsymbol{n}_0^{\alpha} - \boldsymbol{n}_0^{\mathrm{GB}}| - |\boldsymbol{n}_0^{\beta} \cdot \boldsymbol{n}_0^{\mathrm{GB}}|)^2}{b^2}. \tag{17}$$

Note that when the two neighbouring grains have the same crystallographic orientation, the GBD density turns out to be zero. Besides, the amount of grain boundary misorientation together with both lattice orientations determine the compatible GBD density profile. Furthermore, both the length and the direction of the Burgers vector do not need to be updated, as all formulations are evaluated in the reference configuration.

3. Numerical implementation

3.1. Variational formulation

In order to implement the previously discussed crystal plasticity framework in a finite element framework, first, the governing equations must be identified. From Eq. (14), one can conclude that for the determination of the GND density field, the crystallographic slip fields for all slip systems are required. On the other hand, in order to determine the evolution of the crystallographic slip fields through Eq. (4), one needs the current back-stress, which again depends on the GND density field by means of Eqs. (8) and (9). Once those densities are known, all relevant quantities can be determined. The GND densities are therefore chosen to be additional nodal degrees of freedom, accompanied by just as many additional evolution equations. Accordingly, the entire set of governing equations is given by the conventional stress equilibrium condition, evaluated in the undeformed configuration, and Eq. (14), here written in an abbreviated format

$$\boldsymbol{\nabla}_0 \cdot \boldsymbol{T}^{\mathrm{T}} = \boldsymbol{0}, \quad \boldsymbol{T} \equiv \det(\boldsymbol{F})\boldsymbol{\sigma} \cdot \boldsymbol{F}^{-\mathrm{T}}, \tag{18}$$

$$\rho_{\mathrm{GND}}^{\xi} = \rho_{\mathrm{GND}_0}^{\xi} + \boldsymbol{d}_0^{\xi\alpha} \cdot \boldsymbol{\nabla}_0 \gamma^{\alpha} \quad \forall \xi, \tag{19}$$

where $\boldsymbol{T}$ is the first Piola–Kirchhoff stress tensor and where the multipliers $d_{\mathrm{e}}^{\alpha\xi}$ and $d_{\mathrm{s}}^{\alpha\xi}$, the vectors $\boldsymbol{m}_0^{\alpha}$ and $\boldsymbol{p}_0^{\alpha}$, the factor $\frac{1}{b}$, and the corresponding signs are all properly stored in the vectors $\boldsymbol{d}_0^{\xi\alpha}$, using Einstein's summation convention.

The continuity requirements on the displacements as well as the GND densities have to be relaxed over the element boundaries in order to be able to use standard C^0-continuous finite elements. This is accomplished by first multiplying the stress equilibrium and GND density evolution conditions by weighting functions w_u and w_p^ξ, respectively. After integrating both expressions over the volume V_0 of the body in its reference (undeformed) configuration, the divergence theorem is applied and a Newton–Raphson iterative procedure is introduced, which provides the iterative corrections (δT, $\delta\rho_{GND}^\xi$, and $\delta\gamma^\alpha$) to be expressed by linearised functions of the solution estimates (T_*, ρ_{GND}^ξ, and γ_*^α) obtained in the previous iteration

$$\int_{V_0} (\mathbf{\nabla}_0 w_u)^{\mathrm{T}} : \delta T^{\mathrm{T}}\, \mathrm{d}V_0 = \int_{S_0} w_u \cdot t_*\, \mathrm{d}S_0 - \int_{V_0} (\mathbf{\nabla}_0 w_u)^{\mathrm{T}} : T_*^{\mathrm{T}}\, \mathrm{d}V_0, \tag{20}$$

$$\int_{V_0} [w_p^\xi \delta\rho_{GND}^\xi + (\mathbf{\nabla}_0 w_\rho^\xi) \cdot d_0^{\xi\alpha} \delta\gamma^\alpha]\, \mathrm{d}V_0$$
$$= \int_{S_0} w_\rho^\xi \Gamma_{n_*}^\xi\, \mathrm{d}S_0 - \int_{V_0} [w_\rho^\xi (\rho_{GND_*}^\xi - \rho_{GND_0}^\xi) + (\mathbf{\nabla}_0 w_\rho^\xi) \cdot d_0^{\xi\alpha} \gamma_*^\alpha]\, \mathrm{d}V_0 \quad \forall \xi, \tag{21}$$

where at the surface S_0, t_* is the (first Piola–Kirchhoff) surface traction and $\Gamma_{n_*}^\xi$ is a measure for the crystallographic slip in the outward normal direction. In this weak formulation, the equations for the iterative corrections (T_* and γ_*^α) and the iterative updates (δT and $\delta\gamma^\alpha$) are to be expressed and solved as a function of the so-called "independent variables", i.e. the variables which will be selected as the finite element nodal degrees of freedom and their spatial variations. This process is discussed in the next subsection.

3.2. Iterative updates and tangents

The elaborations (at the integration point level) in this subsection are presented under the assumption of plane stress loading conditions. Therefore, the total deformation gradient tensor is written as the additive decomposition

$$F = \overline{F} + \widehat{F}, \tag{22}$$

where $\overline{F}$ only contains the four in-plane components of F and where $\widehat{F}$ contains the three non-zero components energetically associated to the stress components which are enforced to equal zero

$$T \cdot e_0^3 = \mathbf{0}. \tag{23}$$

Here, the initial unit base vector e_0^3 is oriented in the out-of-plane direction. Next to the three degrees of freedom in $\widehat{F}$, and next to $\overline{F}$, the remaining two components of the deformation gradient tensor equal zero. Now, three sets of variables are distinguished. First, the components of $\widehat{F}$ constitute, along with all slip rates $\dot{\gamma}^\alpha$, the entire set of dependent variables. This set is a priori unknown, yet it can be solved as a function of the independent variables $\overline{F}$, ρ_{GND}^ξ, and $r_0^\xi \equiv \mathbf{\nabla}_0 \rho_{GND}^\xi$, which are straightforwardly determined from the intentional nodal degrees of freedom. Together, both sets represent the entire set of state variables, a set which enables the consistent determination of all remaining relevant quantities.

In order to determine the dependent variables at the integration point level, accordingly, the following conditions must be satisfied

$$f\,(\overline{F}, \rho_{GND}^\xi, r_0^\xi, \widehat{F}, \dot{\gamma}^\alpha) = \mathbf{0}, \tag{24}$$

$$g^\alpha(\overline{F}, \rho_{GND}^\xi, r_0^\xi, \widehat{F}, \dot{\gamma}^\alpha) = 0 \quad \forall \alpha, \tag{25}$$

where Eq. (24) is actually a formal representation of Eq. (23), taking into account that the stress T is a priori unknown and is therefore considered to be related to all state variables. Furthermore, Eq. (25) is a

representation of the slip laws in Eq. (4), where Eq. (5) is substituted for the effective stress, again depending on the second Piola–Kirchhoff stress through Eqs. (2), (1), (3) and depending on the back-stress tensor via Eqs. (7)–(9), and where Eq. (6) is substituted for the slip system strength, again depending on Eqs. (12) and (13).

The system of strongly non-linear equations above —Eqs. (24) and (25)— requires an iterative solution procedure at the material point level. Resultingly, the dependent variables are unambiguously determined from the independent variables, which can formally be written as

$$\widehat{\boldsymbol{F}} = \widehat{\boldsymbol{F}}(\overline{\boldsymbol{F}}, \rho_{\mathrm{GND}}^{\xi}, \boldsymbol{r}_0^{\xi}), \tag{26}$$

$$\dot{\gamma}^{\alpha} = \dot{\gamma}^{\alpha}(\overline{\boldsymbol{F}}, \rho_{\mathrm{GND}}^{\xi}, \boldsymbol{r}_0^{\xi}). \tag{27}$$

The macroscopic iterative updates $\boldsymbol{T}_*$ and γ_*^{α}, as required in Eqs. (20) and (21), are solved accordingly by the same iteration process at the material point level. Similar to $\widehat{\boldsymbol{F}}$ and $\dot{\gamma}^{\alpha}$, $\boldsymbol{T}_*$ and γ_*^{α} *also primarily* dependent on the independent variables.

Now, after consistent linearisation of the crystal plasticity framework and the accompanying plane stress condition, the iterative corrections $\delta\boldsymbol{T}$ and $\delta\gamma^{\alpha}$ at the macroscopic level (cf. Eqs. (20) and (21)) can be written as a function of the iterative variations of all independent variables

$$\delta\boldsymbol{T} = \left.\frac{\partial\boldsymbol{T}}{\partial\overline{\boldsymbol{F}}}\right|_{\rho_{\mathrm{GND}}^{\xi}, \boldsymbol{r}_0^{\xi}} : \delta\overline{\boldsymbol{F}} + \left.\frac{\partial\boldsymbol{T}}{\partial\rho_{\mathrm{GND}}^{\xi}}\right|_{\overline{\boldsymbol{F}}, \boldsymbol{r}_0^{\xi}} \delta\rho_{\mathrm{GND}}^{\xi} + \left.\frac{\partial\boldsymbol{T}}{\partial\boldsymbol{r}_0^{\xi}}\right|_{\overline{\boldsymbol{F}}, \rho_{\mathrm{GND}}^{\xi}} \cdot \delta\boldsymbol{r}_0^{\xi}, \tag{28}$$

$$\delta\gamma^{\alpha} = \left.\frac{\partial\gamma^{\alpha}}{\partial\overline{\boldsymbol{F}}}\right|_{\rho_{\mathrm{GND}}^{\xi}, \boldsymbol{r}_0^{\xi}} : \delta\overline{\boldsymbol{F}} + \left.\frac{\partial\gamma^{\alpha}}{\partial\rho_{\mathrm{GND}}^{\xi}}\right|_{\overline{\boldsymbol{F}}, \boldsymbol{r}_0^{\xi}} \delta\rho_{\mathrm{GND}}^{\xi} + \left.\frac{\partial\gamma^{\alpha}}{\partial\boldsymbol{r}_0^{\xi}}\right|_{\overline{\boldsymbol{F}}, \rho_{\mathrm{GND}}^{\xi}} \cdot \delta\boldsymbol{r}_0^{\xi}, \tag{29}$$

where the subscripts next to the vertical bars indicate that the specified variables are kept constant. Here, it is acknowledged that the constitutive formulations of the quantities $\boldsymbol{T}$ and γ^{α} primarily depend on the chosen independent variables $\overline{\boldsymbol{F}}$, $\rho_{\mathrm{GND}}^{\xi}$ and $\boldsymbol{r}_0^{\xi}$, yet secondarily also on the (a priori unknown) dependent variables $\overline{\boldsymbol{F}}$ and $\dot{\gamma}^{\alpha}$. However, this secondary dependence does not involve explicit formulations that can be extracted (as already pointed out, Eqs. (26) and (27) imply the iterative solution of Eqs. (24) and (25)). Therefore, in order to explicitly determine the partial derivatives in Eqs. (28) and (29), those secondary dependencies have to be taken into account.

First, with the purpose of abbreviating the formulations exploiting the secondary dependencies, consider the following definitions

$$\underset{\sim}{\Pi} = \begin{bmatrix} \boldsymbol{T} \\ \gamma^{\alpha} \end{bmatrix}, \quad \underset{\sim}{\Xi} = \begin{bmatrix} \overline{\boldsymbol{F}} \\ \rho_{\mathrm{GND}}^{\xi} \\ \boldsymbol{r}_0^{\xi} \end{bmatrix}, \quad \underset{\sim}{\Psi} = \begin{bmatrix} \widehat{\boldsymbol{F}} \\ \dot{\gamma}^{\alpha} \end{bmatrix}, \quad \underset{\sim}{\Phi} = \begin{bmatrix} \boldsymbol{f} \\ g^{\alpha} \end{bmatrix}, \tag{30}$$

where all components of the tensor and vector quantities, and the complete set of the slip system and dislocation density related quantities, are properly stored in the columns, incorporating the primary unknowns ($\underset{\sim}{\Pi}$), the independent variables ($\underset{\sim}{\Xi}$), the dependent variables ($\underset{\sim}{\Psi}$), and the constitutive conditions ($\underset{\sim}{\Phi}$). Eqs. (28) and (29) can now be summarised by

$$\delta\underset{\sim}{\Pi} = \frac{\mathrm{d}\underset{\sim}{\Pi}}{\mathrm{d}\underset{\sim}{\Xi}} \delta\underset{\sim}{\Xi}, \tag{31}$$

where the matrix $\frac{\mathrm{d}\underset{\sim}{\Pi}}{\mathrm{d}\underset{\sim}{\Xi}}$ contains all relevant partial derivatives. Next, the components of this matrix are elaborated by making a clear distinction between the independent variables and the dependent variables

$$\frac{\mathrm{d}\underset{\sim}{\Pi}}{\mathrm{d}\underset{\sim}{\Xi}} = \frac{\mathrm{d}\underset{\sim}{\Pi}}{\mathrm{d}\underset{\sim}{\Xi}}\bigg|_{\underset{\sim}{\Psi}} + \frac{\mathrm{d}\underset{\sim}{\Pi}}{\mathrm{d}\underset{\sim}{\Psi}}\bigg|_{\underset{\sim}{\Xi}} \frac{\mathrm{d}\underset{\sim}{\Psi}}{\mathrm{d}\underset{\sim}{\Xi}},$$

(32)

and an exercise which allows for the explicit determination of the entries in $\frac{\partial\underset{\sim}{\Pi}}{\partial\underset{\sim}{\Xi}}\big|_{\underset{\sim}{\Psi}}$ and $\frac{\partial\underset{\sim}{\Pi}}{\partial\underset{\sim}{\Psi}}\big|_{\underset{\sim}{\Xi}}$.

The total derivative $\frac{\mathrm{d}\underset{\sim}{\Psi}}{\mathrm{d}\underset{\sim}{\Xi}}$ of the dependent variables with respect to the independent variables in Eq. (32) cannot be determined explicitly. Instead, this derivative follows from the consideration that the requirements in Eqs. (24) and (25) must be satisfied

$$\delta\underset{\sim}{\Phi} = \frac{\mathrm{d}\underset{\sim}{\Phi}}{\mathrm{d}\underset{\sim}{\Xi}}\delta\underset{\sim}{\Xi} = \underset{\sim}{0},$$

(33)

that is, for all variations of the independent variables

$$\frac{\mathrm{d}\underset{\sim}{\Phi}}{\mathrm{d}\underset{\sim}{\Xi}} = \frac{\partial\underset{\sim}{\Phi}}{\partial\underset{\sim}{\Xi}}\bigg|_{\underset{\sim}{\Psi}} + \frac{\partial\underset{\sim}{\Phi}}{\partial\underset{\sim}{\Psi}}\bigg|_{\underset{\sim}{\Xi}} \frac{\mathrm{d}\underset{\sim}{\Psi}}{\mathrm{d}\underset{\sim}{\Xi}} = \underline{0},$$

(34)

where the partial derivatives in $\frac{\partial\underset{\sim}{\Phi}}{\partial\underset{\sim}{\Xi}}\big|_{\underset{\sim}{\Psi}}$ and $\frac{\partial\underset{\sim}{\Phi}}{\partial\underset{\sim}{\Psi}}\big|_{\underset{\sim}{\Xi}}$ can again be derived explicitly, which were actually already required for the material point Newton Raphson iteration procedure for the solution of Eqs. (24) and (25). The remaining derivatives can now be extracted according to

$$\frac{\mathrm{d}\underset{\sim}{\Psi}}{\mathrm{d}\underset{\sim}{\Xi}} = -\left(\frac{\partial\underset{\sim}{\Phi}}{\partial\underset{\sim}{\Psi}}\bigg|_{\underset{\sim}{\Xi}}\right)^{-1}\frac{\partial\underset{\sim}{\Phi}}{\partial\underset{\sim}{\Xi}}\bigg|_{\underset{\sim}{\Psi}}.$$

(35)

Finally, the solution estimates and iterative corrections of the primary unknowns, i.e. $\boldsymbol{T}_*$, γ_*^α, $\delta\boldsymbol{T}$, and $\delta\gamma^\alpha$ in Eqs. (20) and (21), are determined as a function of the nodal degrees of freedom and their spatial variations through Eq. (31).

The presented equations are formulated schematically, yet their elaboration only requires the straightforward determination of the partial derivatives in $\frac{\partial\underset{\sim}{\Pi}}{\partial\underset{\sim}{\Xi}}|_{\underset{\sim}{\Psi}}$, $\frac{\partial\underset{\sim}{\Pi}}{\partial\underset{\sim}{\Psi}}|_{\underset{\sim}{\Xi}}$, $\frac{\partial\underset{\sim}{\Phi}}{\partial\underset{\sim}{\Xi}}|_{\underset{\sim}{\Psi}}$, and $\frac{\partial\underset{\sim}{\Phi}}{\partial\underset{\sim}{\Psi}}|_{\underset{\sim}{\Xi}}$, which would be too comprehensive to include in this work. It is remarked that the time integration schemes required to compute γ^α from Eq. (4) and $\rho_{\mathrm{SSD}}^\alpha$ from Eq. (12) can be chosen arbitrarily between fully explicit and fully implicit.

3.3. Finite element formulation

In order to systematically compute an approximate solution of Eqs. (20) and (21), for arbitrary geometries and boundary conditions, the volume V_0 of the configuration is subdivided in finite elements, whose contributions are subsequently added in a standard manner. Within each element e (having volume V_0^e and boundary surface S_0^e), the unknown fields of the nodal variables and weighting functions, as well as their spatial variations, are approximated by their (global) nodal values (stored in $\underset{\sim}{u}$ and $\underset{\sim}{\rho}_{\mathrm{GND}}$), multiplied by their corresponding interpolation functions (stored in $\underline{N}_u^e$ and $\underline{N}_\rho^e$) or the spatial derivatives thereof (stored in $\underline{B}_u^e$ and $\underline{B}_\rho^e$). Furthermore, the components and indices of $\boldsymbol{d}_0^{\xi\alpha}$ are stored per element in $\underline{D}^e$, and following the procedures from Section 3.2, the iterative estimations of the first Piola–Kirchhoff stress tensor

and the crystallographic slips (stored in $\underset{\sim}{T}^e_*$ and $\underset{\sim}{\gamma}^e_{\text{GND}*}$) can be computed in each material point, based on the nodal degrees of freedom, as well as their iterative corrections (stored in $\delta\underset{\sim}{T}^e$ and $\delta\underset{\sim}{\gamma}^e$)

$$\delta\underset{\sim}{T}^e = \underline{C}^e_1\underline{B}^e_u\delta\underset{\sim}{u} + (\underline{C}^e_2\underline{N}^e_\rho + \underline{C}^e_3\underline{B}^e_\rho)\delta\underset{\sim}{\rho}_{\text{GND}}, \tag{36}$$

$$\delta\underset{\sim}{\gamma}^e = \underline{C}^e_4\underline{B}^e_u\delta\underset{\sim}{u} + (\underline{C}^e_5\underline{N}^e_\rho + \underline{C}^e_6\underline{B}^e_\rho)\delta\underset{\sim}{\rho}_{\text{GND}}, \tag{37}$$

where $\delta\underset{\sim}{u}$ and $\delta\underset{\sim}{\rho}_{\text{GND}}$ are the iterative corrections for the nodal displacement and GND density values, and where the matrices $\underline{C}^e_1$, $\underline{C}^e_2$, $\underline{C}^e_3$, $\underline{C}^e_4$, $\underline{C}^e_5$, and $\underline{C}^e_6$, represent the derivatives as specified in Eqs. (28) and (29) or equivalently Eq. (31), evaluated separately for each element.

After following the standard Galerkin approach and taking into account that both Eqs. (20) and (21) must be satisfied for any admissible weighting function, the following system of equations is established, comprising the discrete force balance and discretised GND density evolution conditions.

$$\begin{bmatrix} \underline{K}_{uu} & \underline{K}_{u\rho} \\ \underline{K}_{\rho u} & \underline{K}_{\rho\rho} \end{bmatrix} \begin{bmatrix} \delta\underset{\sim}{u} \\ \delta\underset{\sim}{\rho}_{\text{GND}} \end{bmatrix} = \begin{bmatrix} \underset{\sim}{r}^u \\ \underset{\sim}{r}^\rho \end{bmatrix}, \tag{38}$$

where

$$\underline{K}_{uu} = \sum_e \int_{V^e_0} \underline{B}^{e\mathrm{T}}_u \underline{C}^e_1 \underline{B}^e_u \, \mathrm{d}V^e_0, \tag{39}$$

$$\underline{K}_{u\rho} = \sum_e \int_{V^e_0} \underline{B}^{e\mathrm{T}}_u (\underline{C}^e_2\underline{N}^e_\rho + \underline{C}^e_3\underline{B}^e_\rho) \, \mathrm{d}V^e_0, \tag{40}$$

$$\underline{K}_{\rho u} = \sum_e \int_{V^e_0} \underline{B}^{e\mathrm{T}}_\rho \underline{D}^e \underline{C}^e_4 \underline{B}^e_u \, \mathrm{d}V^e_0, \tag{41}$$

$$\underline{K}_{\rho\rho} = \sum_e \int_{V^e_0} [\underline{N}^{e\mathrm{T}}_\rho \underline{N}^e_\rho + \underline{B}^{e\mathrm{T}}_\rho \underline{D}^e (\underline{C}^e_5\underline{N}^e_\rho + \underline{C}^e_6\underline{B}^e_\rho)] \, \mathrm{d}V^e_0, \tag{42}$$

$$\underset{\sim}{r}_u = \sum_e \int_{S^e_0} \underline{N}^{e\mathrm{T}}_u \underset{\sim}{t}^e_* \, \mathrm{d}S^e_0 - \sum_e \int_{V^e_0} \underline{B}^{e\mathrm{T}}_u \underset{\sim}{T}^e_* \, \mathrm{d}V^e_0, \tag{43}$$

$$\underset{\sim}{r}_\rho = \sum_e \int_{S^e_0} \underline{N}^{e\mathrm{T}}_\rho \underset{\sim}{\Gamma}^e_{n_*} \, \mathrm{d}S^e_0 \cdots$$
$$- \sum_e \int_{V^e_0} [\underline{N}^{e\mathrm{T}}_\rho \underline{N}^e_\rho (\underset{\sim}{\rho}^e_{\text{GND}*} - \underset{\sim}{\rho}_{\text{GND}_0}) + \underline{B}^{e\mathrm{T}}_\rho \underline{D}^e \underset{\sim}{\gamma}^e_*] \, \mathrm{d}V^e_0, \tag{44}$$

where the boundary terms $\underset{\sim}{t}^e_*$ and $\underset{\sim}{\Gamma}^e_{n_*}$ only have to be specified on element boundaries (S^e_0) coinciding with the outer boundary of the body (S_0). This system is solved by iteratively updating the nodal estimations $\underset{\sim}{u}_*$ and $\underset{\sim}{\rho}_{\text{GND}*}$ with corrections $\delta\underset{\sim}{u}$ and $\delta\underset{\sim}{\rho}_{\text{GND}}$, a process which is repeated until an appropriate convergence criterion is satisfied, i.e. until the right-hand side becomes sufficiently small.

Additionally, the grain boundaries can be regarded to be a part of that outer boundary. To accomplish this, the local finite elements must be uncoupled by means of placing double nodes at the grain boundaries,

of which the displacements are again tied by specifying dependencies in order to maintain the polycrystal sample consistent. That leaves the GND densities or the herewith associated forces to be specified, corresponding to Dirichlet (essential) or Neumann (natural) boundary conditions, respectively.

As the initial GND densities —here representing the GBD densities— can be determined from the crystallographic lattice mismatch (cf. Section 2.3), these can subsequently be prescribed at the nodes on *both* sides of the grain boundaries (i.e. Dirichlet boundary conditions). In order not to disturb the GND density evolution during deformation, the associated initial GND density field is determined by a separate finite element computation on beforehand. During that separate computation, the displacements at the outer boundaries are fixed to zero and at the grain boundary nodes, the GND densities are prescribed to evolve gradually (i.e. linearly, in 15 steps) until the desired value is attained. The resulting GND density field (integration point values) is adopted to serve as the initial GND density field in the actual deformation process simulations.

The total amount of *individual* GBD's necessary to account for lattice incompatibility across the grain boundaries is determined by the initial configuration, and is therefore solely dependent on the initial lattice mismatch. However, during the initial separate finite element computation, the GBD *densities* —as being nodal variables— are inherently spread over a certain area near the grain boundaries. Given the fact that the amount of individual GND's should not change, and the numerical observation that the *relative* GBD density variation between the grain boundary and core is size independent, the dislocation density to be prescribed at the grain boundary nodes ($\rho_{\text{node}_0}^{\xi}$) should follow a relation like (cf. Eqs. (15) and (17))

$$\rho_{\text{node}_0}^{\xi} = \frac{\kappa}{d} \sqrt{\rho_{\text{GND}_0}^{\xi}}, \tag{45}$$

where κ is a dimensionless material constant and d is the grain diameter.

Next, during the finite element simulations of the deformation process, the plastic shear in the grain boundary normal directions is enforced to equal zero (i.e. Neumann boundary conditions), which actually corresponds to the obstruction of crystallographic slip across the grain boundaries. Finally, free boundaries are modelled by enforcing the GND density to vanish locally. Both boundary conditions are quite realistic and constitute a physically based description of crystallographic boundaries.

4. Simulations

The computational implementation of the model under plane stress conditions as discussed in Section 3 has been applied to simulate the size dependent constitutive behaviour of the polycrystal sample which is depicted in Fig. 2. The sample, consisting of 12 grains, is subdivided into 265 linear finite elements, with 379 nodes (4 nodes per element) and 20 degrees of freedom per node (2 displacements and 18 GND densities) resulting in a total number of 7580 degrees of freedom. In addition, the incorporation of double nodes at the grain boundaries requires the account for 176 displacement dependencies in order to kinematically couple the individual grains. Moreover, the entire system of equations is solved using full numerical integration, i.e. 4 integration points per element.

For all simulations, the random crystallographic orientations of the 12 grains are kept equal for all simulated sample sizes and are visualised in Fig. 3. Furthermore, the grain boundary normal directions are chosen parallel to the sample plane. The displacement boundary conditions are presented in Fig. 2, where u_1 is prescribed such that the associated macroscopic strain rate remains fixed at 0.001 s^{-1} (up to a total strain of 0.01 in 175 increments, in the interest of curtailing computation time). The remaining boundary conditions, related to the additional degrees of freedom, i.e. the nodal GND densities or alternatively, the corresponding plastic shear components in the direction perpendicular to the grain boundaries or free surfaces, are attributed as already explained at the end of Section 3. Furthermore, an initial GND density field is supposed to represent the GBD densities, related to the specific grain boundary lattice mismatches, a
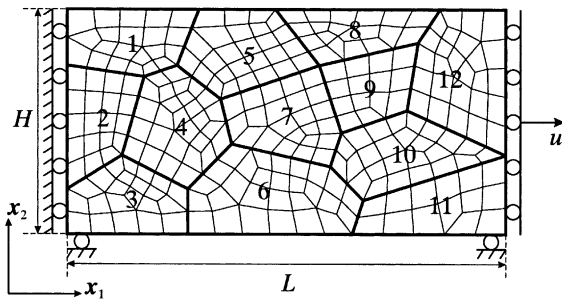
Fig. 2. Geometry and classical displacement boundary conditions with respect to the simulations of the FCC polycrystal sample with length L and height H in tension; the remaining boundary conditions and dependencies are explained in the text.
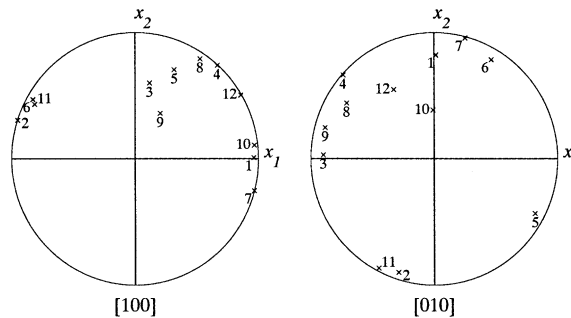

Fig. 3. Equal area projection pole figures with the 12 basic crystallographic lattice directions.

procedure which has also been discussed in Section 3. The sample lengths L are taken to equal 10^{-3}, $10^{-\frac{8}{3}}$, $10^{-\frac{7}{3}}$ and 10^{-2} m (equivalent to 1.0, 2.2, 4.6 and 10 mm, respectively). Once the sample size decreases, the intragranular (plastic) inhomogeneities are expected to increase, along with the GND densities, which then play a significant role in strengthening the specimen through short- and long-range interactions. Finally, the temperature (in Eq. (4)) is taken 300 K and the material constants of FCC copper (12 slip systems and SSD types, 18 GND types) are specified in Table 3.

In the following, the results for the specimen lengths 1 and 10 mm are compared in order to achieve a clear insight into the various size effects. First, a scalar measure for the dislocation densities is evaluated, which is taken to equal the Euclidean norm of all SSD or GND density contributions. Note that the dislocation sign of the GND densities is not considered in this respect, as such would be too comprehensive for 18 different types. The distribution of the density measure for the SSD's is presented in Fig. 4, from which it can be concluded that the difference in order of magnitude between both length scales remains rather small.

When regarding the distribution of that same measure, however now evaluated for the GND densities in Fig. 5, a clear distinction between both scales can be observed. In the case of the small sample, the order of magnitude of the GND densities is roughly 5 times less than the SSD counterpart, whereas the GND densities of the large sample are almost negligible. The first explanation for this is the fact that, as a result of Eq. (45), the total amount of GBD dislocations necessary to account for lattice incompatibility across the grain boundaries is automatically spread over a larger area in Fig. 5(b), resulting in an initial difference

Table 3
Constitutive parameters for FCC copper; partly adopted from Evers et al. (2002) or fitted on the data in that work, and partly taken from elsewhere (cf. the footed references); the coefficients a_0, a_1, a_2 and a_3 are entries in the dislocation interaction matrix $A^{\alpha\xi}$, which is documented by Franciosi and Zaoui (1982) and quantified for copper by Cuitiño and Ortiz (1992); the coefficients h_0, h_1, h_2 and h_3 are entries in $H^{\alpha\xi}$, whose values for copper are adopted from Tabourot et al. (1997)

Parameter	Symbol	Magnitude	Unit	Used in Eq.
Young's modulus	E	144	GPa	(2)
Poisson's ratio	v	0.33	–	(2) and (8)
Reference plastic strain rate	$\dot{\gamma}_0$	0.001	s^{-1}	(4)
Rate sensitivity exponent[a]	m	0.05	–	(4)
Boltzmann's constant	k	1.38×10^{-23}	$J\,K^{-1}$	(4)
Reference activation energy[b]	G_0	4.54×10^{-20}	J	(4)
Strength parameter	c	0.3	–	(6)
Shear modulus	μ	54.2	GPa	(6), (8) and (9)
Burgers vector length[c]	b	0.256	nm	(6), (8), (9), (12), (14) and (17)
Interaction coefficient	a_0	0.06	–	(6) (in $A^{\alpha\xi}$)
Interaction coefficient	a_1/a_0	5.7	–	(6) (in $A^{\alpha\xi}$)
Interaction coefficient	a_2/a_0	10.2	–	(6) (in $A^{\alpha\xi}$)
Interaction coefficient	a_3/a_0	16.6	–	(6) (in $A^{\alpha\xi}$)
Radius GND evaluation area	R	3.16×10^{-6}	m	(8) and (9)
Critical annihilation length[d]	y_c	1.6	nm	(12)
Initial SSD density[e]	ρ_{SSD_0}	1.0×10^{12}	m^{-2}	(12)
Material constant[f]	K	10	–	(13)
Immobilisation coefficient	h_0	0.2	–	(13) (in $H^{\alpha\xi}$)
Immobilisation coefficient	h_1	0.3	–	(13) (in $H^{\alpha\xi}$)
Immobilisation coefficient	h_2	0.4	–	(13) (in $H^{\alpha\xi}$)
Immobilisation coefficient	h_3	1.0	–	(13) (in $H^{\alpha\xi}$)
GBD parameter	κ	0.1	–	(45)

[a] Tabourot et al. (1997).
[b] Ashmawi and Zikry (2000).
[c] Cuitiño and Ortiz (1992).
[d] Essmann and Mughrabi (1979).
[e] Cuitiño and Ortiz (1992).
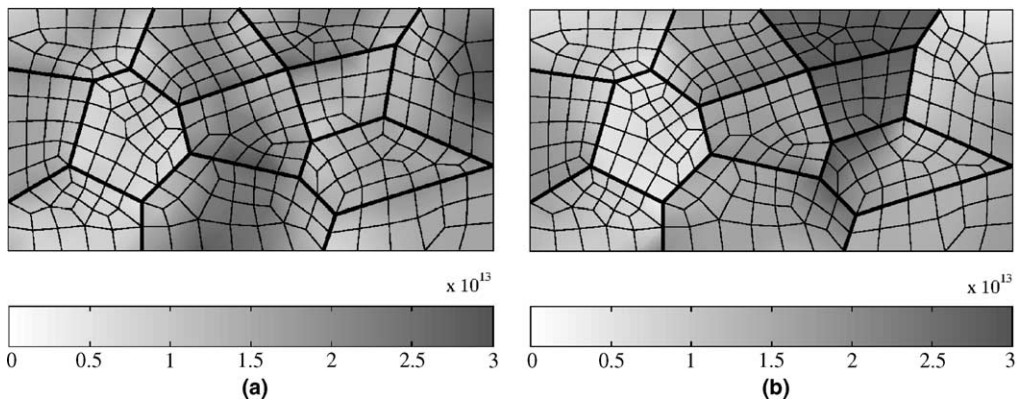[f] Sabar et al. (2002).

Fig. 4. Distribution of the SSD density measure for two sample lengths at an equivalent strain of $\varepsilon = 0.01$. (a) $L = 1.0$ mm, (b) $L = 10$ mm.
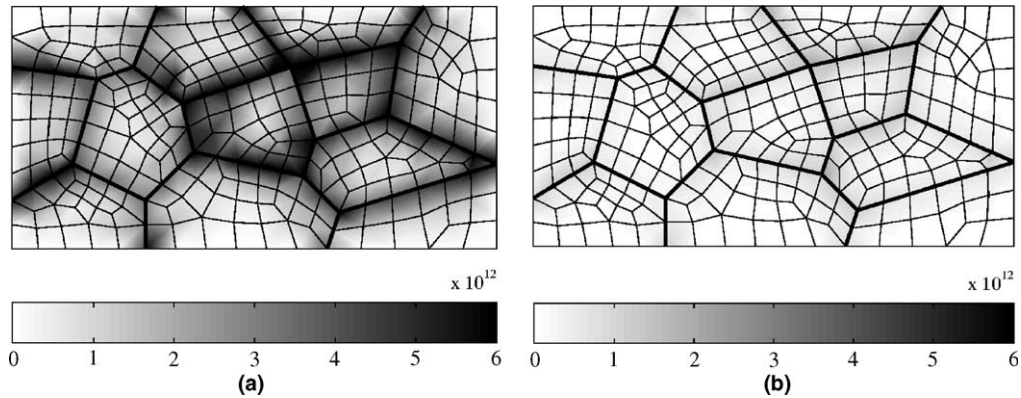
Fig. 5. Distribution of the GND density measure for two sample lengths at an equivalent strain of $\varepsilon = 0.01$. (a) $L = 1.0$ mm, (b) $L = 10$ mm.

between both GND density distributions. The second explanation for the larger GND density magnitude in Fig. 5(a) is the fact that, during deformation, the plastic inhomogeneity between the grain core and the boundaries —where the slip is obstructed— has to be overcome within a much smaller distance (factor 10) in the $L = 1$ mm case. According to Eq. (14), the GND densities automatically increase when the plastic slip gradients increase, which does not only result in an increased slip resistance through Eq. (6), but also in an increased back-stress contribution via Eqs. (8), (9) and (7).

In order to examine the development of the dislocation density measures during the course of the deformation and to recover their actual value, they are evaluated along a cross-section at half the sample height for various equivalent logarithmic strain values $\varepsilon = \sqrt{\frac{2}{3}\boldsymbol{\varepsilon} : \boldsymbol{\varepsilon}}$, where $\boldsymbol{\varepsilon} = \ln(\boldsymbol{U})$ and $\boldsymbol{U}$ is the right stretch tensor. Herewith, 5 grain boundaries are intersected, of which the positions are graphically represented by the dashed vertical lines. In Fig. 6(a) and (b), it can be clearly observed that the SSD densities evolve slightly more in the core regions of the grains than in the grain boundary regions. This can be attributed to the SSD density evolution in Eq. (12), which is higher in regions where the crystallographic slip is less impeded. As already emphasized above, no significant differences arise between both length scales.

The GND density profiles along the intersection for both length scales are shown in Fig. 7(a) and (b). Here indeed a huge difference is observed, where the GND densities of the large sample are approximately 7 times smaller than those of the small sample. In contrast to the SSD profiles, the GND densities increase near the grain boundary and decrease toward the grain cores and toward the GND-free outer surface, entirely in agreement with the expectations. Moreover, the relative *evolution* of the GND densities during deformation is considerably smaller than the evolution of the SSD densities, which triggers the question whether such GND profiles would also arise in absence of any initial GND densities. As a verification of this, the same simulations have been performed, yet without the grain boundary dislocation densities. The accompanying profiles of the GND density measure are shown in Fig. 8(a) and (b). In the right part of the sample, the GND density measure quickly increases to similar levels, while the densities on the left remain a little smaller. However, the tendency of the GND densities to increase toward the grain boundaries remains intact, which can therefore be attributed to the additional boundary conditions that obstruct plastic slip in the direction perpendicular to those boundaries.

Finally, the stress–strain responses for the various sample sizes under consideration are evaluated. For bulk grains, it is expected that the flow stress will follow the Hall–Petch relation (Hall, 1951; Petch, 1953; Armstrong et al., 1962)
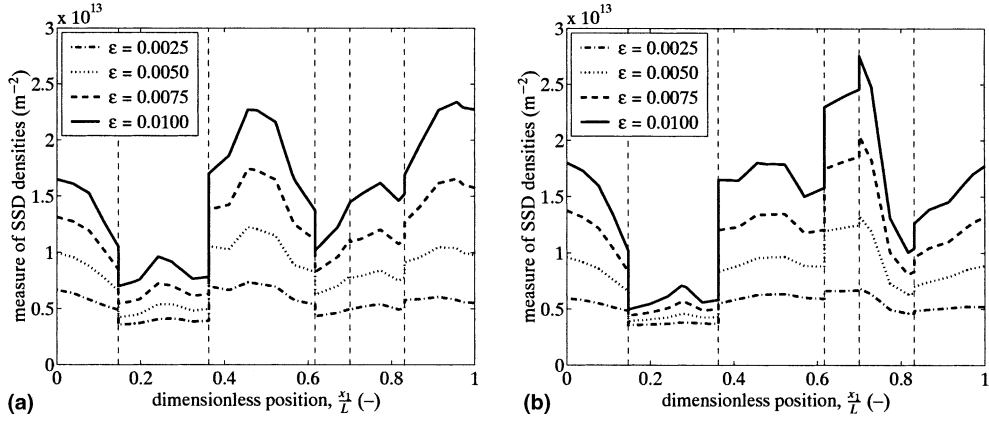
Fig. 6. Profile of the measure for the SSD densities along the x_1-direction for increasing deformation ε, evaluated at half the sample height; the vertical dashed lines indicate the x_1-positions of the grain boundary intersections. (a) $L = 1.0$ mm, (b) $L = 10$ mm.
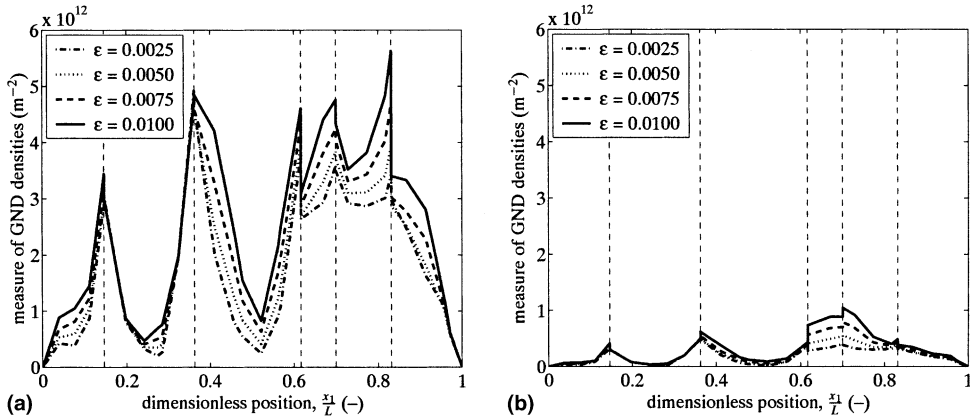

Fig. 7. Profile of the measure for the GND densities along the dimensionless x_1-direction for increasing deformation ε, evaluated at half the sample height; the vertical dashed lines indicate the x_1-positions of the grain boundary intersections. (a) $L = 1.0$ mm, (b) $L = 10$ mm.

$$\sigma(\varepsilon) = \sigma_0(\varepsilon) + k(\varepsilon)d^{-n}, \tag{46}$$

where ε is the equivalent logarithmic strain measure defined previously and σ is the equivalent von Mises stress according to

$$\sigma = \sqrt{\frac{3}{2}\boldsymbol{\sigma}_d : \boldsymbol{\sigma}_d}, \quad \boldsymbol{\sigma}_d = \boldsymbol{\sigma} - \frac{1}{3}\mathrm{tr}(\boldsymbol{\sigma})\boldsymbol{I} \tag{47}$$

while σ_0 is the flow stress in the absence of any size effects, i.e. corresponding to the imaginary situation of an infinitely large sample (in this case realized by enforcing all nodal GND densities to equal zero). Both the equivalent logarithmic strain measure and the von Mises stress measure are volume-averaged over the entire sample. Furthermore, k and n are the Hall–Petch slope and exponent, respectively.
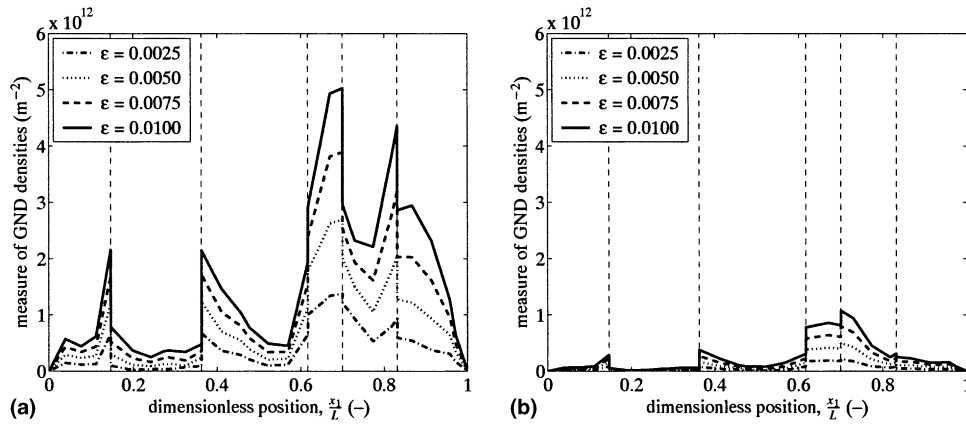
Fig. 8. Profile of the measure for the GND densities along the dimensionless x_1-direction for increasing deformation ε, evaluated at half the sample height; in contrast to Figs. 4–7, here, the GBD densities have been omitted; the vertical dashed lines indicate the x_1-positions of the grain boundary intersections. (a) $L = 1.0$ mm, (b) $L = 10$ mm.

The response results are presented in Fig. 9(a) and (b), for both the cases with and without an initial GND density field, respectively. An obvious size effect can be distinguished, not only during plastic deformation, but moreover also at the onset of yielding. This latter effect is clearly the result of the presence of the GBD densities and is often observed in reality (e.g. Carreker and Hibbard, 1953). In order to quantify this grain size effect, the Hall–Petch relation in Eq. (46) is considered. However, it is noted that the particular polycrystal specimen in Fig. 2 deals with a much higher free surface fraction (with respect to the amount of grain boundaries) than the bulk polycrystals for which the Hall–Petch relation is actually intended. Besides, due to the limited number of grains, the specific crystallographic orientations may influence the results.

In order to find the Hall–Petch parameters, i.e. the Hall–Petch slope k and the exponent n, the value of $\sigma_0(\varepsilon)$ is taken according to the stress–strain profile as simulated for the sample of (imaginary) infinitely large dimensions. Next, the parameters are determined in such a way that the total accumulated difference between the simulated stress–strain curves and the curves following from the Hall–Petch relation is minimized
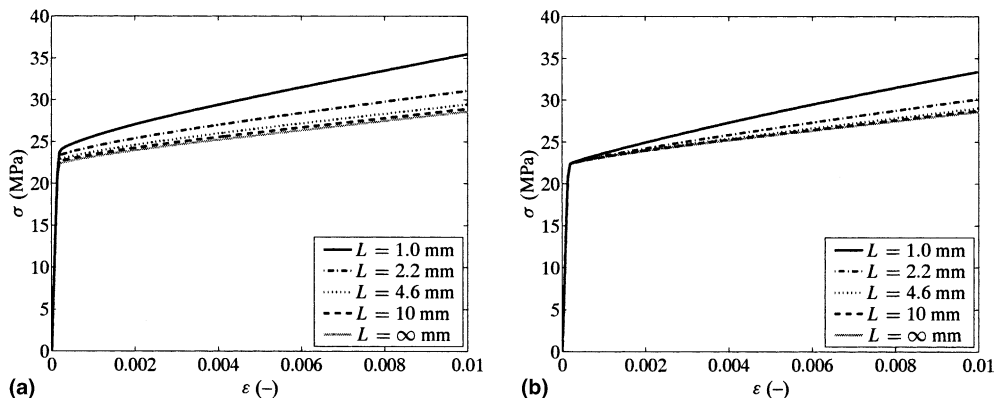

Fig. 9. Stress–strain curves for various sample lengths L; Hall–Petch exponent $n = 1.50$. (a) With GBD densities. (b) Without GBD densities.
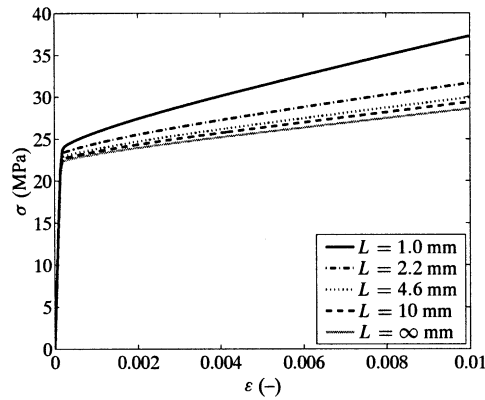
Fig. 10. Stress–strain curves for various sample lengths L, taking into account GBD densities and obstructing plastic deformation near the outer surfaces; Hall–Petch exponent $n = 1.19$.

in a least squares sense, following Evers et al. (2002). For this procedure, it is assumed that n is a constant and that k may vary as a function of the equivalent logarithmic strain ε. The best fit of the Hall–Petch relation on *both* the data of Fig. 9(a) and (b) is achieved using a Hall–Petch exponent of $n = 1.50$. Both figures reveal the same Hall–Petch exponent because of the fact that the influence of the GBD density field is merely a superposition, which does not significantly disturb the dislocation density evolutions as such. The value for n achieved is larger than the values mostly reported in the literature, i.e. $0.3 \leqslant n \leqslant 1.0$, but it is remarked again, this might be caused by the enlarged free surface effect. In order to circumvent this effect, additional simulations have been performed, which consider the free surfaces to be artificial grain boundaries, i.e. by obstructing the crystallographic slip contribution in their outward normal direction. The resulting stress–strain response is presented in Fig. 10 and results in a Hall–Petch exponent of $n = 1.19$.

5. Conclusions

A non-local crystal plasticity framework has been developed, which incorporates the distinct interactions of various types of dislocation densities. This has been accomplished by including a phenomenological flow rule at the slip system level, which depends on an effective resolved shear stress and a slip resistance term. The first one is composed of the ordinary Schmid stress, yet in this case "corrected" by a newly developed back-stress measure, which represents the long-range interactions that are characteristic of GND density fields, because of their specific dislocation sign and relatively large range of influence. Moreover, it brings about a kinematic hardening contribution and includes dependencies between various slip systems based on their spatial orientation. The second term —the slip resistance— depends on the short-range interactions between all dislocations present in the material (and therefore capable of obstructing the ongoing plastic deformation). This term comprises various interactions between SSD's and GND's on different slip systems, i.e. based on their spatial orientation. Whereas the SSD densities are controlled by a "generation-annihilation" evolution equation adopted from literature, the GND densities follow directly from the spatial gradients of crystallographic slip. Finally, a simplified formulation has been presented for the determination of grain boundary dislocation densities, based on the crystallographic lattice mismatch at the grain boundaries. These densities are used as a qualitative measure for an initial GND density field.

The implementation of the entire framework in a finite element environment incorporates the consideration of two governing equations, i.e. the ordinary stress equilibrium condition and the GND–plastic slip

coupling. Next to formulating their variational expression, linearising them and discretising the governing quantities within a finite element context, the solution procedure for solving the strongly non-linear set of equations at the integration point level has been presented, along with a pragmatic approach for determining the consistent tangential relations which are necessary to solve the global system of equations iteratively. The extra nodal degrees of freedom —the GND densities— allow for the specification of various additional boundary conditions which closely approach reality, i.e. dislocation free outer surfaces, strongly obstructed plastic deformation between grains, and an initial GND density field near the grain boundaries.

The mechanical response of a polycrystal sample under plane stress conditions has been simulated for various sample sizes, where the grain configuration and crystallographic orientations remain unaltered. The SSD density field appears to be nearly size independent, where the largest SSD densities are found in the crystal core, related to the unhindered crystallographic slip in that region. Furthermore, the GND field is strongly size dependent, as the plastic inhomogeneities between the grain boundaries and the cores have to be accommodated by the GND field within a varying distance for the different sample sizes. This strengthening effect manifests itself in a size dependent flow stress, in addition to which the initial GND density field causes the (initial) yield stress to be size dependent.

References

Acharya, A., 2001. A model of crystal plasticity based on the theory of continuously distributed dislocations. Journal of the Mechanics and Physics of Solids 49, 761–784.

Aifantis, E.C., 1987. The physics of plastic deformation. International Journal of Plasticity 3, 211–247.

Armstrong, R., Codd, I., Douthwaite, R.M., Fetch, N.J., 1962. The plastic deformation of polycrystalline aggregates. Philosophical Magazine 8, 45–58.

Arsenlis, A., Parks, D.M., 2002. Modeling the evolution of crystallographic dislocation density in crystal plasticity. Journal of the Mechanics and Physics of Solids 50, 1979–2009.

Asaro, R.J., Rice, J.R., 1977. Strain localization in ductile single crystals. Journal of the Mechanics and Physics of Solids 25, 309–338.

Ashby, M.F., 1970. The deformation of plastically non-homogeneous materials. Philosophical Magazine 21, 399–424.

Ashmawi, W.M., Zikry, M.A., 2000. Effects of grain boundaries and dislocation density evolution on large strain deformation modes in fcc crystalline materials. Journal of Computer-Aided Materials Design 7, 55–62.

Ashmawi, W.M., Zikry, M.A., 2003. Single void morphological and grain-boundary effects on overall failure in F.C.C. polycrystalline systems. Materials Science and Engineering A 343, 126–142.

Bassani, J.L., 2001. Incompatibility and a simple gradient theory of plasticity. Journal of the Mechanics and Physics of Solids 49, 1983–1996.

Becker, R., Panchanadeeswaran, S., 1995. Effects of grain interactions of deformation and local texture. Acta Metallurgica et Materialia 43, 2107–2119.

Bronkhorst, C.A., Kalidindi, S.R., Anand, L., 1992. Polycrystalline plasticity and the evolution of crystallographic texture in FCC metals. Philosophical Transactions of the Royal Society of London A 341, 443–477.

Carreker, R.P., Hibbard, W.R., 1953. Tensile deformation of high-purity copper as a function of temperature, strain rate, and grain size. Acta Metallurgica 1, 654–663.

Cermelli, P., Gurtin, M.E., 2002. Geometrically necessary dislocations in viscoplastic single crystals and bicrystals undergoing small deformations. International Journal of Solids and Structures 39, 6281–6309.

Cottrell, A.H., 1961. Dislocations and Plastic Flow in Crystals. Oxford University Press, London.

Cuitiño, A.M., Ortiz, M., 1992. Computational modelling of single crystals. Modelling and Simulation in Materials Science and Engineering 1, 225–263.

Dai, H., Parks, D.M., 1997. Geometrically-necessary dislocation density and scale-dependent crystal plasticity. In: Khan, A.S. (Ed.), Proceedings of Plasticity '97: The Fifth International Symposium on Plasticity and its Current Applications. Neat Press, Juneau, Alaska, pp. 17–18.

Essmann, U., Mughrabi, H., 1979. Annihilation of dislocations during tensile and cyclic deformation and limits of dislocation densities. Philosophical Magazine A 40, 731–756.

Evers, L.P., Parks, D.M., Brekelmans, W.A.M., Geers, M.G.D., 2002. Crystal plasticity model with enhanced hardening by geometrically necessary dislocation accumulation. Journal of the Mechanics and Physics of Solids 50, 2403–2424.

Evers, L.P., Brekelmans, W.A.M., Geers, M.G.D., in press. Non-local crystal plasticity model with intrinsic SSD and GND effects. Journal of the Mechanics and Physics of Solids.

Fleck, N.A., Hutchinson, J.W., 1997. Strain gradient plasticity. Advances in Applied Mechanics 33, 295–361.

Fleck, N.A., Muller, G.M., Ashby, M.F., Hutchinson, J.W., 1994. Strain gradient plasticity: theory and experiment. Acta Metallurgica et Materialia 42, 475–487.

Franciosi, P., Zaoui, A., 1982. Multislip in F.C.C. crystals; a theoretical approach compared with experimental data. Acta Metallurgica 30, 1627–1637.

Gao, H., Huang, Y., 2003. Geometrically necessary dislocation and size-dependent plasticity. Scripta Materialia 48, 113–118.

Gao, H., Huang, Y., Nix, W.D., Hutchinson, J.W., 1999. Mechanism-based strain gradient plasticity—I. Theory. Journal of the Mechanics and Physics of Solids 47, 1239–1263.

Gavriljuk, V.G., Berns, H., Escher, C., Glavatskaya, N.I., Sozinov, A., Petrov, Y.N., 1999. Grain boundary strengthening in austenitic nitrogen steels. Materials Science and Engineering A 271, 14–21.

Gray III, G.T., Chen, S.R., Vecchio, K.S., 1999. Influence of grain size on the constitutive response and substructure evolution of MONEL 400. Metallurgical and Materials Transactions A 30, 1235–1247.

Gurtin, M.E., 2002. A gradient theory of single-crystal viscoplasticity that accounts for geometrically necessary dislocations. Journal of the Mechanics and Physics of Solids 50, 5–32.

Hall, E.O., 1951. The deformation and aging of mild steel: iii. discussion of results. Proceedings of the Physical Society of London B 64, 747–753.

Hansen, N., 1982. Flow stress and grain size dependence of non-ferrous metals and alloys. In: Yield, Flow and Fracture of Polycrystals, vol. XI. Applied Science Publishers, London, pp. 311–350.

Harder, J., 1999. A crystallographic model for the study of local deformation processes in polycrystals. International Journal of Plasticity 15, 605–624.

Hutchinson, J.W., 1976. Bounds and self-consistent estimates for creep of poly-crystalline materials. Proceedings of the Royal Society of London A 348, 101–127.

Kalidindi, S.R., Bronkhorst, C.A., Anand, L., 1992. Crystallographic texture evolution in bulk deformation processing of fcc metals. Journal of the Mechanics and Physics of Solids 40, 537–569.

Kocks, U.F., 1970. The relation between polycrystal deformation and single crystal deformation. Metallurgical Transactions 1, 1121–1144.

Kocks, U.F., 2001. Realistic constitutive relations for metal plasticity. Materials Science and Engineering A 317, 181–187.

Kröner, E., 1962. Dislocations and continuum mechanics. Applied Mechanics Review 15, 599–606.

Kubin, L.P., Canova, G., Condat, M., Devincre, B., Pontikis, V., Brechet, Y., 1992. Dislocation microstructures and plastic flow: a 3D simulation. Solid State Phenomena 23 & 24, 455–472.

Lavrentev, F.F., 1980. The type of dislocation interaction as the factor determining work hardening. Materials Science and Engineering 46, 191–208.

Lee, E.H., 1969. Elastic-plastic deformation at finite strains. Journal of Applied Mechanics 36, 1–6.

Mandel, J., 1974. Thermodynamics and plasticity. In: Delgado Domingos, J.J., Nina, M.N.R., Whitelaw, J.H. (Eds.), Proceedings of the International Symposium on Foundations of Continuum Thermodynamics. Bussaco, Portugal, pp. 283–311.

Mughrabi, H., 2001. On the role of strain gradients and long-range internal stresses in the composite model of crystal plasticity. Materials Science and Engineering A 317, 171–180.

Narutani, T., Takamura, J., 1991. Grain-size strengthening in terms of dislocation density measured by resistivity. Acta Metallurgica et Materialia 39, 2037–2049.

Nemat-Nasser, S., Luqun, N., Okinaka, T., 1998. A constitutive model for fcc crystals with application to polycrystalline OFHC copper. Mechanics of Materials 30, 325–341.

Nix, W.D., Gao, H., 1998. Indentation size effects in crystalline materials: a law for strain gradient plasticity. Journal of the Mechanics and Physics of Solids 46, 411–425.

Nye, J.F., 1953. Some geometrical relations in dislocated crystals. Acta Metallurgica 1, 153–162.

Peirce, D., Asaro, R.J., Needleman, A., 1982. An analysis of non-uniform and localized deformation in ductile single crystals. Acta Metallurgica 30, 1087–1119.

Petch, N.J., 1953. The cleavage strength of polycrystals. Journal of the Iron and Steel Institute 174, 25–28.

Rice, J.R., 1971. Inelastic constitutive relations for solids: an internal variable theory and its application to metal plasticity. Journal of the Mechanics and Physics of Solids 19, 433–455.

Sabar, H., Berveiller, M., Favier, V., Berbenni, S., 2002. A new class of micro-macro models for elastic-viscoplastic heterogeneous materials. International Journal of Solids and Structures 39, 3257–3276.

Shu, J.Y., Fleck, N.A., 1999. Strain gradient crystal plasticity: size-dependent deformation of bicrystals. Journal of the Mechanics and Physics of Solids 47, 297–324.

Shu, J.Y., Fleck, N.A., Van der Giessen, E., Needleman, A., 2001. Boundary layers in constrained plastic flow: comparison of nonlocal and discrete dislocation plasticity. Journal of the Mechanics and Physics of Solids 49, 1361–1395.

Sluys, L.J., Estrin, Y., 2000. The analysis of shear banding with a dislocation based gradient plasticity model. International Journal of Solids and Structures 37, 7127–7142.

Steinmann, P., 1996. Views on multiplicative elastoplasticity and the continuum theory of dislocations. International Journal of Engineering Science 34, 1717–1735.

Stölken, J.S., Evans, A.G., 1998. A microbend test method for measuring the plasticity length scale. Acta Metallurgica et Materialia 46, 5109–5115.

Tabourot, L., Fivel, M., Rauch, E., 1997. Generalised constitutive laws for f.c.c. single crystals. Materials Science and Engineering A 234–236, 639–642.

Thompson, A.W., Baskes, M.I., Flanagan, W.F., 1973. The dependence of polycrystal work hardening on grain size. Acta Metallurgica 21, 1017–1032.

Worthington, P.J., Smith, E., 1964. The formation of slip bands in polycrystalline 3% silicon iron in the pre-yield microstrain region. Acta Metallurgica 12, 1277–1281.